Effects of Carbon Variation on Microstructure Evolution in Weld Heat-Affected Zone of Nb-Ti Microalloyed Steels

XIAOPING MA, XUEDA LI, BRIAN LANGELIER, BAPTISTE GAULT, SUNDARESA SUBRAMANIAN, and LAURIE COLLINS

We investigated the effects of C concentration variation from 0.028 to 0.058 wt pct on microstructure of the coarse grained heat-affected zone (CGHAZ) of low heat input girth welded Ti-Nb microalloyed steels by using electron microscope and atom probe tomography. It is found that the CGHAZ microstructure exhibits a systematic response to C variation. Increased C raises the temperature for precipitation of NbC. This leads to coarser (Ti, Nb)N-Nb(C, N) but finer delayed strain-induced NbC in the high-C steel than in the low-C steel. Fine strain-induced NbC are ineffective in preventing austenite grain coarsening in CGHAZ due to their fast dissolution upon heating. For a given inter-particle spacing originally determined by (Ti, Nb)N particles, increased epitaxial growth of Nb(C, N) on pre-existing (Ti, Nb)N in the high-C steel results in a smaller austenite grain size of 34 μm in the CGHAZ of the high-C steel than that of 52 μm in the low-C steel. Increased C promotes a microstructure consisting of bainitic lath structure with C Cottrell atmospheres at dislocation debris and martensitic layers of 30 to 100 nm in thickness at inter-lath boundaries in the CGHAZ. Increased C promotes configuration of crystallographic variants belonging to different Bain groups in the neighbors, preferentially twin-related variant pairs within a bainite packet.

https://doi.org/10.1007/s11661-018-4751-8

I. INTRODUCTION

EXCELLENT combinations of strength and toughness are obtained in modern pipe line steels by thermo-mechanically controlled processing, in conjunction with Ti and Nb microalloying, to produce a fine, uniform microstructure.[1,2] However, the microstructure obtained in the base metal is upset by the thermal cycles brought about by the welding during pipe making and joining, resulting in areas of poor toughness in the heat-affected zone (HAZ).[3] One of the causes of embrittlement is the formation of undesirable microstructures resulting from weld thermal cycles and the base chemical composition of the steel.[4] Since the HAZ microstructure is heterogeneous and has many sub-zones, it is very difficult to establish the relative contribution of each sub zone to the properties, but the area most frequently highlighted in literature for impairing toughness is the coarse grained HAZ (CGHAZ).

CGHAZ refers to the region immediately adjacent to the weld fusion line, where the base metal was subjected to a high thermal cycle peak temperature above the solvus for microalloying carbo-nitrides and significant austenite grain coarsening occurs. The extent of austenite grain coarsening depends on the thermal cycle experienced, and the chemical composition of the steel, as well as the size and dispersion of second phase particles and their potential for dissolution.[5-7] In the absence of thermo-mechanical deformation, the resulting microstructure morphology and crystallography in CGHAZ upon subsequent cooling depend on the temperature at which phase transformation occurs, which, in turn is determined by the hardenability and the cooling rate.[8] Additionally, martensite-austenite (MA) constituent has been identified as a distinct microstructural feature influencing HAZ toughness.[4,9,10] It is widely accepted that coarse MA

XIAOPING MA is with the Department of Materials Science and Engineering, McMaster University, Hamilton, Canada, L8S 4L7, Canada and also with Algoma Steel Inc., Sault Ste. Marie, P6A 7B4, Canada. Contact e-mail: xiaoping.ma@algoma.com XUEDA LI is with the College of Mechanical and Electronic Engineering, China University of Petroleum (East China), Qingdao, 266580, China. BRIAN LANGELIER and SUNDARESA SUBRAMANIAN are with the Department of Materials Science and Engineering, McMaster University. BAPTISTE GAULT is with the Department of Microstructure Physics and Alloy Design, Max-Planck-Institut für Eisenforschung GmbH, Max-Planck-Straße 1, Düsseldorf, 40237, Germany. LAURIE COLLINS is with EVRAZ North America, Regina, S4P 3C7, Canada.

Manuscript submitted December 17, 2017.
Article published online July 5, 2018

deteriorates toughness by initiating brittle micro-cracks, either by the cracking of MA particles or their decohesion with the matrix, in accordance with the Cottrell–Petch model for brittle fracture.[11] Refinement of MA is thus important to improve HAZ toughness, by preclusion of brittle crack initiation.

Although each of the abovementioned morphological and crystallographic parameter has been extensively investigated,[1-3,5,6] studies have mostly been based on laboratory thermal simulation. In real-weld HAZs, control of microstructure is far more complex due to its sensitivity to both base chemical composition and welding parameters. A change in chemistry and/or welding parameter would lead to a significant system variation in hierarchical microstructure evolution in CGHAZ, including Ti/Nb carbo-nitrides precipitation and dissolution, austenite grain coarsening, subsequent microstructure transformation, and associated crystallographic orientation configuration as influenced by variant selection. The objective of the present work is to investigate the chemistry effects by studying how variation in C from 0.028 to 0.058 wt pct in base chemistry affects morphology and crystallography of the microstructure in CGHAZ of real girth welded X80 grade Ti-Nb microalloyed pipeline steels.

II. MATERIALS AND EXPERIMENTAL PROCEDURES

Two industrial Steckel mill processed 10.4-mm-thick X80 grade line pipe steels were used in the present investigation. The chemical compositions of these two steels are given in Table I. The steel with the lower C content is referred to low-C steel, while the steel with the higher C content is referred to high-C steel. The pipe joint welding was carried out by low heat input (3 to 7 kJ/cm) multi-pass girth welding.

After optical metallography, electron back scatter diffraction (EBSD) was performed on a JEOL SEM7000 at 20 kV. Conventional (CM12, 120 kV) and high-resolution (FEI Titan, 80 to 300 kV) transmission electron microscopes (TEMs) were used for the characterization of HAZ microstructure morphology and crystallography, and nano-scale precipitates in the base metal and the HAZ of the two steels. While EBSD characterization covers several prior austenite grains, the scale of TEM characterization occurs within a prior austenite grain, but covering several bainitic laths or ferrite grains. Energy dispersive X-ray spectroscopy (EDS INCA) installed on the TEM was used to analyze the chemical composition of precipitates. Atom probe tomography (APT) was used to investigate precipitate dissolution through characterization of the micro-chemistry in the CGHAZ. Thermodynamic analysis of precipitation of stoichiometric Ti and Nb carbo-nitrides was carried out using Hillert and Staffansson's model for sublattice regular solution.[12]

Carbon extraction replicas were prepared on the well-polished sample surface lightly etched using 4 pct nital for TEM characterization of the original size and dispersion of precipitates in the base metal of the low-C and high-C steels. It is worth noting that the width of the CGHAZ is in the range of 250 and 300 μm. Different techniques involving dimpling, electro polishing, ion milling, focused ion beam (FIB), and nano-milling were used for the specimen preparation in the required locations in the CGHAZ. Thin foils for TEM analysis were prepared by mechanically grinding the HAZ included samples with initial thickness of 400 μm to the thickness of 100 μm and pre-dimpled in the desired locations and then electro-polished with a double-jet Struers Tenupol machine at 228 K (− 45 °C), and 15 V in an electrolyte containing 27 mL perchloric acid and 273 mL alcohol. Ion milling and nano-milling were used to further thin the electro-polished specimens in the desired locations. EBSD was carried out site-specifically on TEM thin foils tiled at 70 deg with step size of 50 and 200 nm at 20 kV. Pole figure analysis was carried out to analyze the EBSD database to distinguish the different packets and Bain groups occurring in transformation product in the HAZ. FIB was used to prepare the specimens for APT using a lift-out procedure described in Reference 13. APT was performed using a Cameca local electrode atom probe 4000X HR. APT experiments were carried out at a base temperature of 60 K in laser pulse mode (λ = 355 nm), with a pulse energy of 60 to 80 pJ, a pulse rate of 250 kHz, and an average detection rate of 0.01 ions/pulse. Reconstructions of APT data were performed using IVAS 3.6.6 software, and established reconstruction protocols.[14]

III. EXPERIMENTAL RESULTS

Figure 1 shows a composite diagram including an optical image of a cross-section of the multi-pass girth weld, a schematic illustration of different sub-zones of the HAZ in the cap region of the weld, and a schematic diagram showing the thermal cycle history of the different sub-zones. As seen in the optical image in Figure 1, the HAZ in the cap region, indicated by a circle, is not affected by the thermal cycles of any subsequent weld pass, thus, it can be treated as the HAZ of single pass weld. The regions marked by green color in the schematic diagram of single-pass weld indicate the

Table I. Chemical Composition of Two Investigated Steels with Lower and Higher C Content in Weight Percenct (At. Pct)

	C	Mn	S	Nb	Ti	N
Low-C Steel	0.028 (0.130)	1.71 (1.73)	0.002 (0.004)	0.089 (0.053)	0.016 (0.018)	0.0075 (0.0298)
High-C Steel	0.058 (0.269)	1.67 (1.69)	0.001 (0.002)	0.088 (0.053)	0.015 (0.017)	0.0075 (0.0298)

Balance: Fe + Cu + Ni + Cr + Mo.

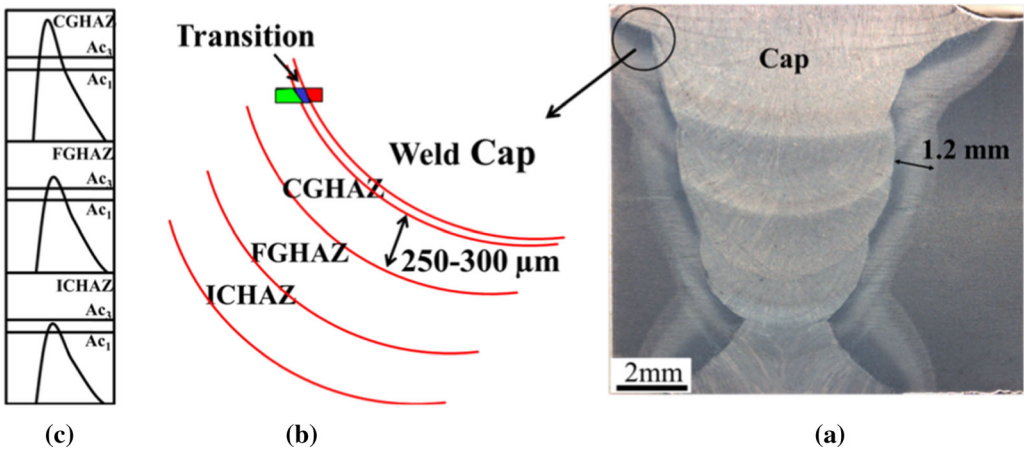

Fig. 1—Composite diagram including (*a*) optical images of multi-pass low heat input girth weld showing specimen location in the HAZ corresponding to single pass welding used in the present investigation, (*b*) schematic illustration showing the different sub-zones of the HAZ in the cap region and the specific location of the specimen examined, (*c*) schematic diagram showing the thermal history of different sub-zones with respect to temperature window of inter-critical region of phase stability of ferrite plus austenite (Color figure online).

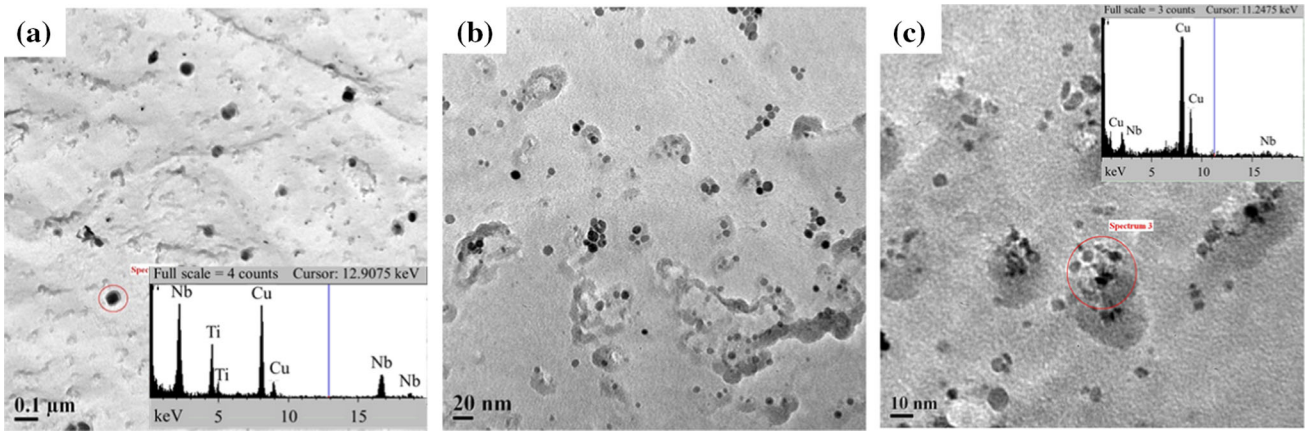

Fig. 2—(*a*) to (*c*) TEM images of the carbon extraction replica showing the precipitates in the base metal of the low-C steel. The EDS inset in (a) shows Nb-Ti rich chemical composition in the precipitates indicated in (a). The EDS inset in (c) confirms the Nb-rich precipitates marked.

location where comprehensive multi-scale, multi-level characterization is carried out.

The experimental observations are analyzed with the focus on understanding the effects that variation in C content in the base composition has on the dissolution of Ti/Nb carbo-nitrides, austenite grain coarsening, hierarchical evolution of the microstructure morphology, and associated crystallographic orientation configuration in the CGHAZ of the two steels.

A. *Effects of C Variation on Behavior of Ti and Nb Carbo-nitrides Precipitation in Base Metal and Dissolution in CGHAZ*

Figures 2 and 3 show TEM characterization results of the precipitates in the base metal of the low-C and high-C steels, respectively. EDS analysis of the precipitates confirms that there are two types of precipitates in both steels: those rich in Ti-Nb and those rich in only Nb. The size of Ti-Nb-rich precipitates in the low-C steel is in the range of 30 to 50 nm, while they are 50 to 80 nm in the high-C steel, as shown in Figures 2(a) and 3(a). However, the low-C steel exhibits the larger Nb-rich precipitates in the range of 5 to 16 nm than the high-C steel, which contains Nb-rich precipitates mostly smaller than 5 nm, as shown in Figures 2(b), (c) and 3(c), respectively.

Site-specific preparation of a carbon extraction replica to characterize the precipitates remaining in the CGHAZ was too difficult to achieve, due to the small size of the CGHAZ associated with the low heat input girth weld. Thus, TEM thin foil samples, prepared from the CGHAZ immediately adjacent to the fusion lines, are examined instead. From this analysis, only Ti-N-b-rich precipitates are observed. Figures 4(a) and (b) show typical TEM images of Ti-Nb-rich precipitates in the CGHAZ of the low-C steel. No evidence for preservation of the fine Nb-rich precipitates is found in the CGHAZ of both the low-C and high-C steels, indicating that the fine Nb-rich precipitates were dissolved during the thermal cycle.

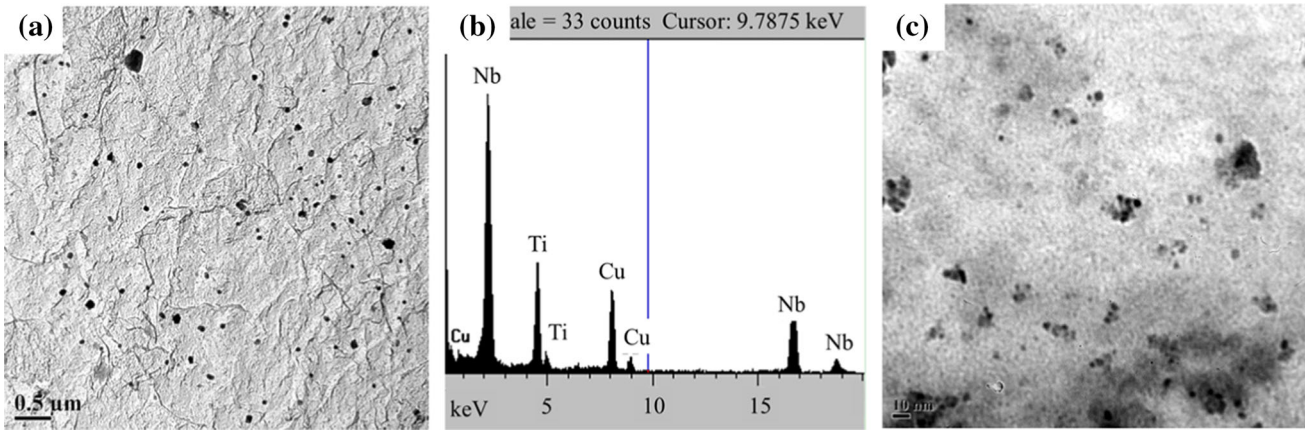

Fig. 3—(*a*) TEM image of the carbon extraction replica showing the Ti-Nb-rich precipitates and (*b*) typical EDS analysis of Ti-Nb-rich precipitates shown in (a), (*c*) TEM image showing fine NbC precipitates in the thin foil sample of the base metal of the high-C steel.

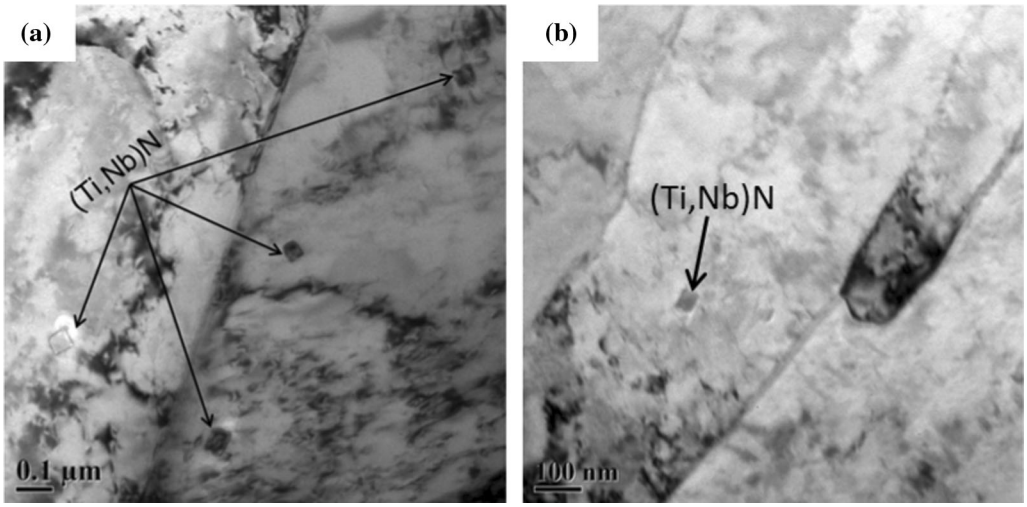

Fig. 4—TEM images of CGHAZ immediately adjacent to fusion line in the low-C steel showing Ti-Nb-rich precipitates in both (*a*) and (*b*), no evident Nb-rich precipitate is seen.

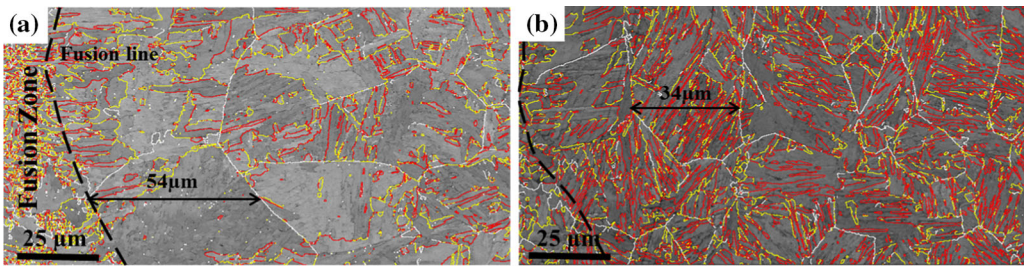

Fig. 5—Kikuchi band contrast map from EBSD characterization (scan step size of 0.2 μm) on CGHAZ in cap region of the multi-pass girth welded (*a*) low-C steel; (*b*) high-C steel with misorientation boundaries above 55 deg indicated by red line, above 45 deg indicated by yellow line, and above 15 deg indicated by white line. The white lines delineate the prior austenite grain boundaries (Color figure online).

The Nb content in solid solution within the CGHAZ of the two steels is investigated by APT, measured immediately adjacent to the fusion lines (see supplementary material for the detailed chemical analysis by APT). Approximately, 0.0547 wt pct solute Nb is revealed in the CGHAZ of the high-C steel, while it is found that about 0.084 wt pct Nb is dissolved in the CGHAZ of the low-C steel.

B. *Austenite Grain Coarsening in the CGHAZ Immediately Adjacent to the Fusion Line*

EBSD characterization at the fusion zone—CGHAZ in the cap region of multi-pass girth weld was carried out. Grain boundaries of different misorientation are highlighted in the Kikuchi band contrast maps shown in Figures 5(a) and (b) for the low-C and high-C steels, respectively. Prior austenite grain boundaries are found to be associated with misorientation angles above 15 deg and below 45 deg. An important aspect of a real-weld HAZ is a decrease in austenite grain size with increasing distance from the fusion line (indicated in Figure 2 by dashed lines) into the base metal. Prior austenite grain sizes are measured in the CGHAZ, within 200 μm from the fusion line. A finer grain size of 34 $\pm$ 5.6 μm is observed in the high-C steel, compared to 52 $\pm$ 11 μm in the low-C steel.

C. *Effects of C Variation on Morphology and Crystallography of Microstructure in the CGHAZ*

Figures 6(a) and (b) present the high-resolution EBSD band contrast maps of the CGHAZ in the cap region in the low-C and high-C steels, respectively. The low-C steel shows a microstructure composed of quasi-polygonal ferrite and a small volume fraction of lath-like structure. The high-C steel exhibits a laminar microstructure with laths growing from austenite grain boundaries and intra-granular needle-like ferrite dividing the lath packets. These different overall CGHAZ microstructure morphologies between the two steels suggest that transformation occurs at a lower temperature in the high-C steel than in the low-C steel. Corresponding to the band contrast maps given in Figures 6(a) and (b), (c) and (d) show the EBSD all Euler maps superimposed with high-angle boundaries above 45 deg indicated by the yellow lines and Σ3 boundary represented by the red lines in the CGHAZ of the two steels, respectively. CGHAZ of the low-C steel shows a non-uniform distribution of high-angle boundaries with large inter-spacing typical of 10 μm. In contrast, CGHAZ of the high-C steel exhibits a uniform dispersion of high-angle boundaries with inter-spacing typically less than 2 μm.

Detailed local observation of the lath-like structure or individual ferrite grains at a fine scale is provided by TEM analysis. Figure 7 gives the TEM images showing quasi-polygonal ferrite [Figure 7(a)] and a small fraction of bainitic lath structure [Figure 7(b)] in the CGHAZ in the low-C steel. TEM examination reveals dislocation debris in bainitic ferrite laths, as shown in Figures 7(b) and (c). The high dislocation density in bainitic ferrite is attributed to the plastic deformation resulting from the displacive mode of transformation.[15-17]

Figures 8(a) through (c) show TEM images of bainitic laths with intermittent MA layers at inter-lath boundaries (30 to 100 nm in thickness) in the CGHAZ of the high-C steel. The average thickness of the bainitic laths is typically 0.5 μm. By comparing the dispersion of the

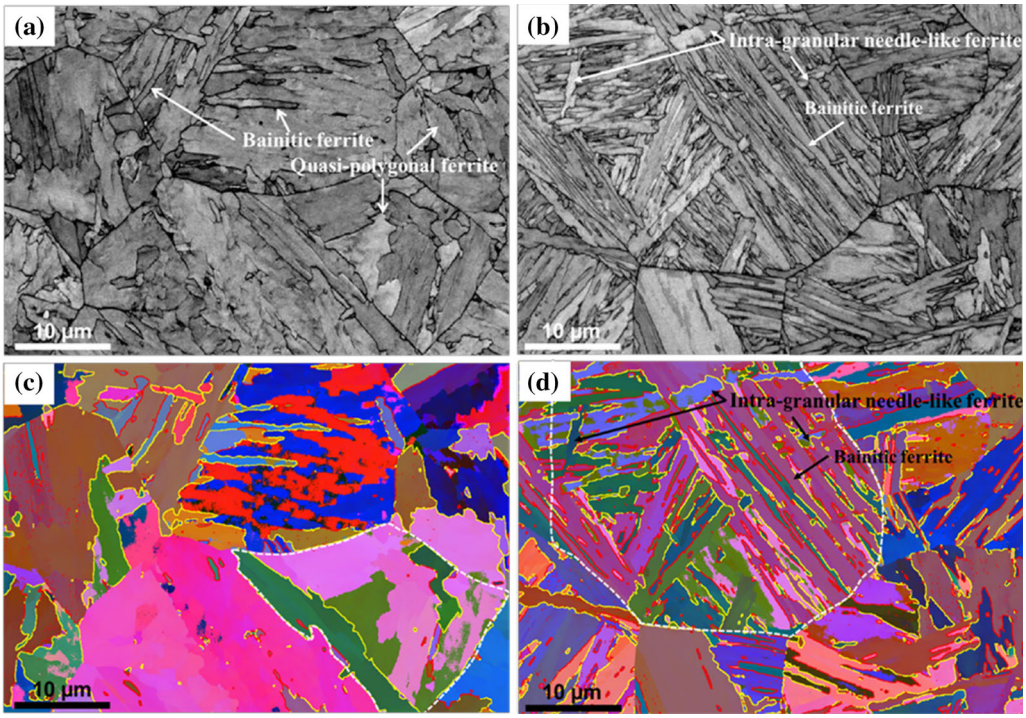

Fig. 6—EBSD Kikuchi band contrast maps of the CGHAZ in the cap region of (*a*) low-C steel showing a complex microstructure composed of lath-like bainite and quasi-polygonal ferrite, (*b*) high-C steel showing austenite grains interspersed with intra-granular needle-like ferrite and bainitic ferrite growing from the austenite grain boundaries; and corresponding all Euler maps showing crystallographic orientation represented by different color and high-angle boundaries above 45 deg indicated by yellow lines and Σ3 coincidence boundaries by red lines: (*c*) low-C steel with a low density and non-uniform dispersion of high-angle boundaries, (*d*) high-C steel with high density and dispersion of high-angle boundaries (Color figure online).

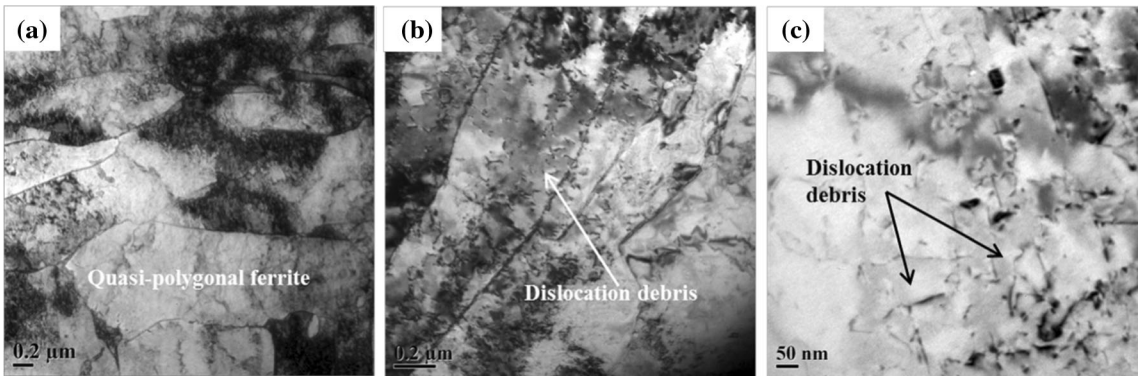

Fig. 7—TEM images of the microstructure in CGHAZ in the low-C steel showing: (*a*) quasi-polygonal ferrite, (*b*) bainitic ferrite laths, (b) and (*c*) a high density of dislocation debris in the bainitic ferrite laths observed at low and high magnifications, respectively.

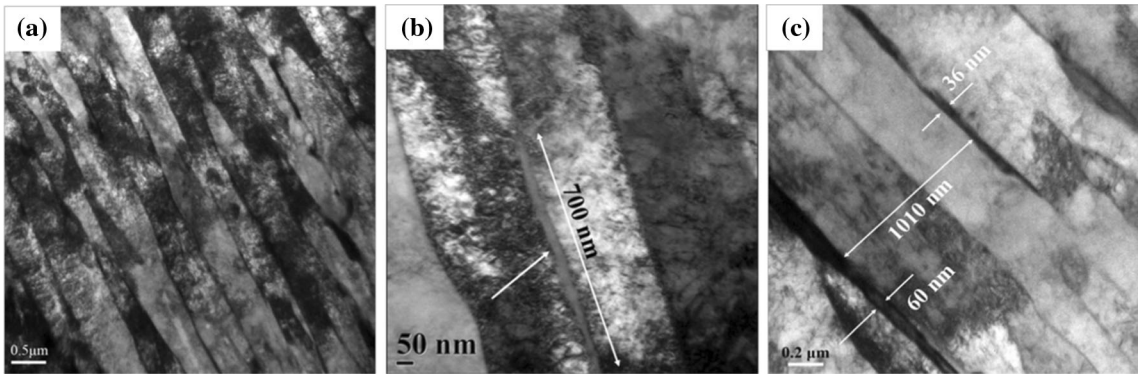

Fig. 8—TEM images of the bainitic microstructure in CGHAZ in the high-C steel, at (*a*) low and (*b*) to (*c*) high magnification.

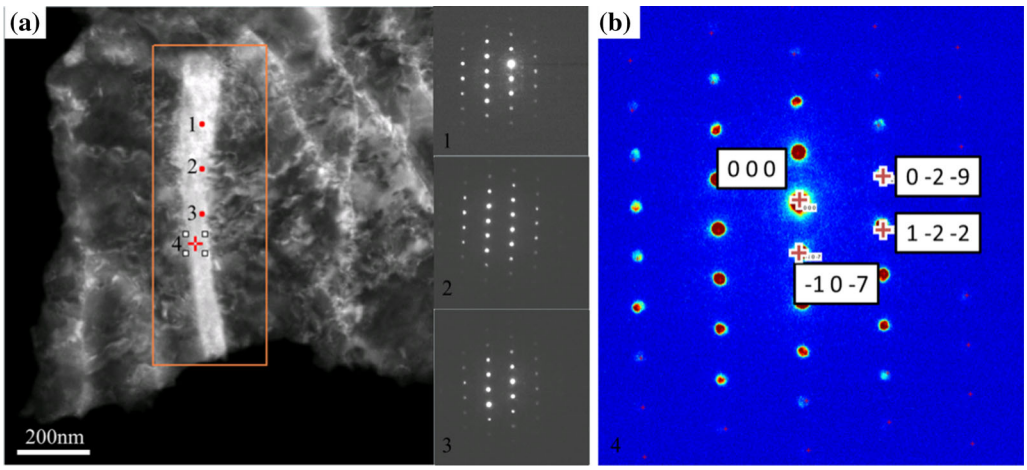

Fig. 9—STEM characterization, (*a*) an image of a MA thin film at a bainitic inter-lath boundary, with marked spots where selected area diffraction was performed and the corresponding diffraction pattern inserted laid-out on the right side of the image, (*b*) the indexed pattern of the diffraction carried out at spot-4 as marked in (a) (Color figure online).

high-angle boundaries in Figure 6(d) with the alignment of the bainitic laths as observed in the TEM images in Figure 8(a), it is seen that a high-angle boundary inter-spacing contains one or more bainitic laths. The bainitic laths contain a high density of dislocations. Analysis of the fine scale of the MA films at inter-lath boundaries is conducted by high-resolution high-angle annular dark-field STEM, with results shown in Figure 9. Figure 9(a) shows a MA layer at bainitic inter-lath boundary, with four marked spots where selected area diffractions were performed. Indexing one of the four similar selected area diffraction patterns indicates a closer match with martensite other than austenite, as shown in Figure 9(b).

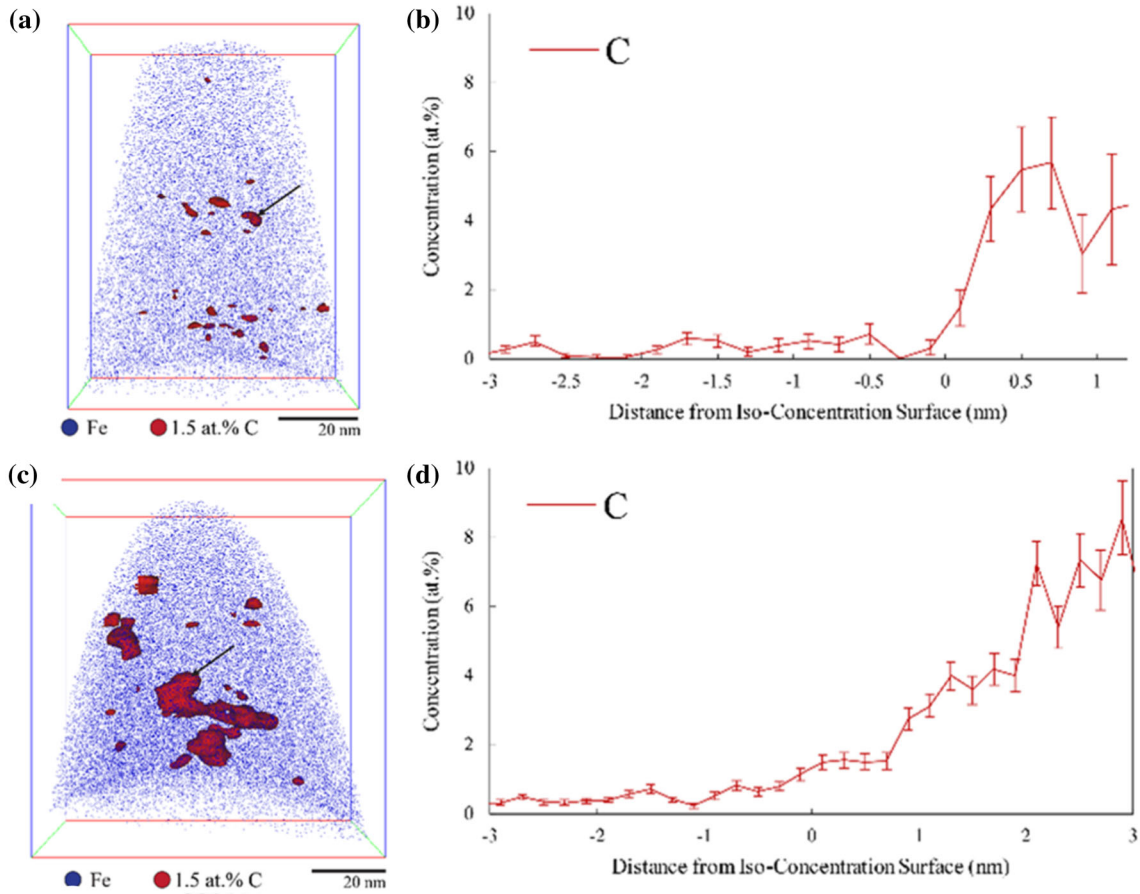

Fig. 10—(*a*) and (*c*) APT reconstruction atomic maps with 1.5 at. pct C iso-concentration surfaces indicated in CGHAZ of the low-C and high-C steels, respectively, (*b*) and (*d*) proxigrams showing C concentration profiles across the largest iso-concentration surfaces in (a) and (c), respectively (shown by arrows), indicating the increase in local C concentration up to 5 to 9 at. pct (Color figure online).

Since a bainitic transformation involves C partitioning, C distribution in the CGHAZ of the two steels was investigated using APT. Figures 10(a) and (b) show the APT reconstruction overlaid with a set of dark red iso-concentration surfaces that encompass regions of the data containing more than 1.5 at. pct C. Due to the irregular shape and distribution of the C-enriched regions in comparison to the martensite films at inter-lath boundaries shown in Figure 9, these C-enriched regions are considered to be trapping of C at dislocation debris as Cottrell atomspheres in bainitic ferrite.[18-20] The chemical composition profiles known as proxigram computed from the iso-concentration surfaces in the low-C and high-C steels are given in Figures 10(c) and (d), respectively. The local C concentration in the Cottrell atmospheres in the two steels is in the range of 5 to 9 at. pct, comparable to the prediction by Cochardt *et al*. of a C saturation of 6 to 7 at. pct in the region of one Burgers vector around the core.[21] It is important to note that the volume of the APT sample is considered large enough to include some fine NbC with a short inter-spacing as shown in Figures 2 and 3, if there were any NbC remaining in CGHAZ; however, no evident Nb-enriched region is seen. This confirms the TEM observation that most of the fine Nb-rich precipitates were dissolved in the CGHAZ in both the low-C and high-C steels. No Ti-Nb-rich precipitate was captured in the volume of materials involved in APT analysis due to the sparse distribution of the Ti-Nb-rich precipitates.

IV. DISCUSSION

A. *Effect of Varying C Content on Precipitation Behavior of Ti-Nb Carbo-nitrides in the Base Metal and Their Dissolution in CGHAZ*

The interpretation of the difference in size and dispersion of Ti-Nb- and Nb-rich precipitates in the base metal between the low-C and high-C steels requires an understanding of the effects of varying C content on thermodynamics and kinetics of NbC precipitation during the controlled thermo-mechanical rolling of the two steels. Figures 11(a) and (b) present the diagrams of the thermodynamic analysis of stoichiometric Ti and Nb carbo-nitride precipitation based on the regular solution model for mixed carbo-nitrides of Ti and Nb for the low-C and high-C steels, respectively. Mixed nitrides of TiN and NbN occur at high temperatures. Since the Ti, Nb, and N contents in the two tested steels are similar, there is no difference in the thermodynamic potential for

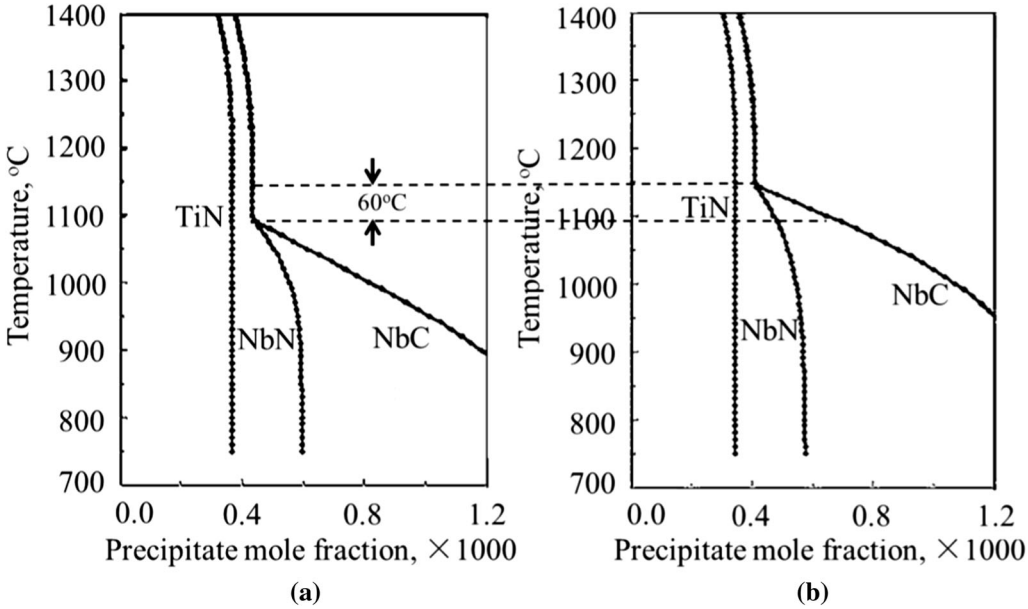

Fig. 11—Thermodynamic calculation of cumulative mole fraction of Ti and Nb carbo-nitrides as a function of temperature in Fe-C-Mn system in (*a*) low-C, (*b*) high-C steels.

precipitation of Ti and Nb nitrides between the two steels. However, the increase in C content from 0.028 to 0.058 wt pct raises the start temperature for precipitation of NbC by 60 K (60 °C) from 1363 K (1090 °C) for the low-C steel to 1423 K (1150 °C) for the high-C steel. Regarding the NbC precipitation kinetics, previous work by Subramanian *et al*. using hot torsion simulation[22] has shown that the epitaxial growth of NbC on pre-existing TiN particles occurs at negligible undercooling in Ti + Nb microalloyed steel, compared with strain-induced precipitation of NbC that occurs at a substantial undercooling [> 100 K (100 °C)] in only Nb microalloyed steel. In the present work, due to the over-stoichiometric ratio of N to Ti in the two steels, excessive N combines with Nb at high temperatures, resulting in (Ti, Nb)N particles. These (Ti, Nb)N particles then act as the substrate for epitaxial growth of Nb(C, N) at equilibrium temperature to form (Ti, Nb)N-Nb(C, N) composite precipitates. The magnitude of the epitaxial growth of Nb(C, N) on (Ti, Nb)N particles depends on the inter-particle spacing of pre-existing (Ti, Nb)N,[23] thermodynamic potential for precipitation of NbC as determined by chemistry, and the diffusivity of Nb (lattice/dislocated pipe diffusion).[24] Since the processing parameters for the two steels by the Steckel mill are the same, it is considered that the distribution of pre-existing (Ti, Nb)N composite precipitates in the two steels is similar. Higher thermodynamic potential for the precipitation of NbC brought about by increased C content in the high-C steel promotes more epitaxial growth of Nb(C, N) on pre-existing (Ti, Nb)N particles when compared to that in the low-C steel. Thus, a larger size of (Ti, Nb)N-Nb(C, N) composite precipitates in the range of 50 to 80 nm is observed in the high-C steel, in comparison with those of 30 to 50 nm in the low-C steel. Hong *et al*. reported that the epitaxial growth of NbC on pre-existing TiN particles delays the strain-induced NbC due to the depletion of solute Nb in the austenite matrix.[25] More epitaxial growth of Nb(C, N) on pre-existing (Ti, Nb)N particles causes a larger extent of depletion of solute Nb in the austenite matrix, leading to a more significant delay in the strain-induced Nb(C, N) at a lower temperature in the processing of the high-C steel compared to the low-C steel. Therefore, the high-C steel exhibits the finer strain-induced Nb(C, N) (< 5 nm) than the low-C steel which contains larger Nb(C, N) of sizes in the range of 5 to 16 nm. The author's recent investigation shows that a complete suppression of strain-induced NbC is feasible by decreasing the inter-particle spacing of TiN-NbC composite as determined originally by TiN particles.[26]

Upon heating by welding, dissolution of Nb carbo-nitrides occurs in the CGHAZ. The site-specific APT characterization of the region in CGHAZ immediately adjacent to the fusion lines as described in Section III–A reveals that 0.0547 wt pct Nb is dissolved into solution in the CGHAZ of the high-C steel. For a given total Nb content of 0.088 wt pct, it indicates that 0.0333 wt pct Nb remains in the precipitates. According to the thermodynamic calculation given in Figure 12(b), 0.0333 wt pct Nb combines with 0.002 wt pct N and 0.0026 wt pct C, providing that niobium-to-N ratio and niobium-to-C ratio in niobium nitride and carbide are stoichiometric. Banerjee *et al*.[5] reported that fine strain-induced Nb(C, N) precipitates undergo complete dissolution even at a heating rate of 1000 K/s to 1623 K (1350 °C) and holding for 0.5 seconds, characteristic of a low heat input girth welding. This is in agreement with the observation reported herein, no evidence for preservation of fine Nb(C, N) is found in the CGHAZ of the two tested steels. Therefore, it is considered that Nb(C,

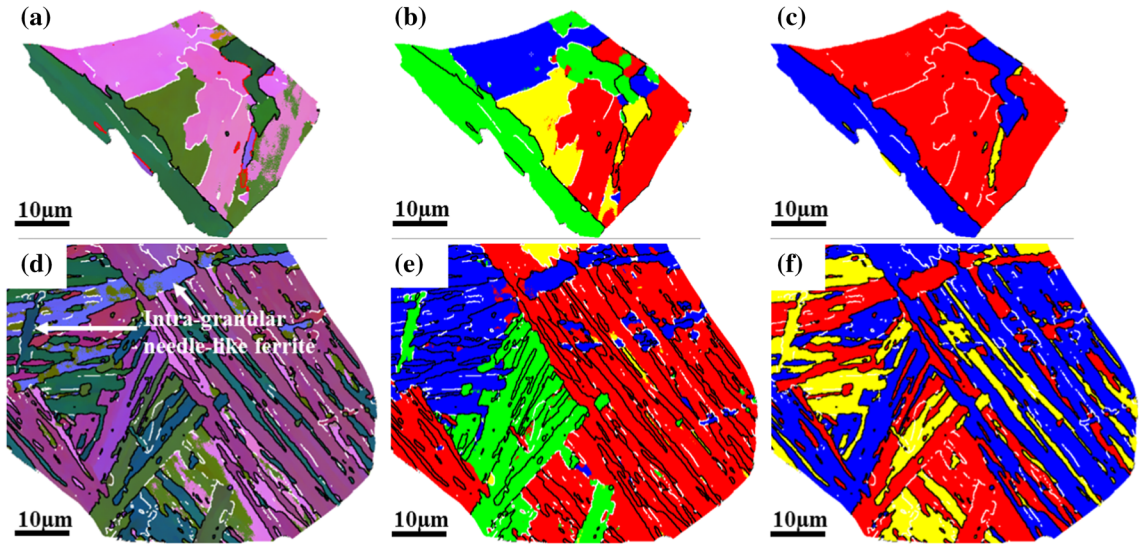

Fig. 12—(*a*) to (*c*) All Euler, packet, and Bain maps of the structure within the austenite grain delineated in Fig. 11(a) in the CGHAZ of the low-C steel, (*d*) to (*f*) all Euler, packet, and Bain maps of the structure within the austenite grain delineated in Fig. 11(b) in the CGHAZ of the high-C steel. The black and white lines in each map indicate grain boundaries with misorientation angle above 45 deg and Σ1 boundaries featured as rotation by 10.5 deg about ⟨110⟩ axis, respectively (Color figure online).

N) remaining in the CGHAZ of the high-C steel is associated with (Ti, Nb)N-Nb(C, N) composite precipitates.[27] Since both the low-C and high-C steels went through the same welding thermal cycle, it is predicted from Figure 12(a) that 0.0836 wt pct Nb is dissolved into solution and 0.0054 wt pct remain in precipitates as NbN associated with (Ti, Nb)N in the CGHAZ of the low-C steel. Actual APT investigation reveals a solute Nb content of 0.088 ± 0.004 wt pct in the CGHAZ of the low-C steel (see Online Appendix 1).

Based on the amount of precipitated Ti and Nb, the volume fraction of precipitates remaining in the CGHAZ of the two investigated steels is calculated to correlate with austenite grain size. All Ti exists in the form of TiN and no dissolution of TiN occurs upon weld reheating due to its high thermodynamic stability. For 0.015 wt pct Ti in TiN and 0.0333 wt pct Nb precipitated as Nb(C, N), taking into account the molar volume of the precipitates and Fe matrix, the volume fraction of TiN and Nb(C, N) is calculated to be 0.00056 and 0.00074, respectively. Thus, the total volume fraction of the (Ti, Nb)N-Nb(C, N) composite precipitates remaining in the CGHAZ of the high-C steel is $f_{(\mathrm{Ti,\ Nb)N-Nb(C,\ }N)} = 0.00056 + 0.00074 = 0.0013$. By the same token, for 0.016 wt pct Ti in TiN and 0.0054 wt pct Nb precipitated in NbN, the total volume fraction of (Ti, Nb)N in CGHAZ of the low-C steel can be calculated as $f_{(\mathrm{Ti,Nb)N}} = 0.00056 + 0.00012 = 0.00068$.

B. *Effect of (Ti, Nb)N-Nb(C, N) Composite Precipitates on Prevention of Austenite Grain Coarsening in CGHAZ*

Banerjee *et al.*[5] reported that the austenite grain size is about 4 to 6 μm after complete phase transformation at around 1173 K (900 °C) at a heating rate (100 to 1000 K/s) typical of low heat input girth welding. Fine austenite grains tend to coarsen rapidly upon continuous heating above 1173 K (900 °C). The driving force for austenite grain growth and coarsening is the capillarity:

$$F_{\mathrm{DRI}} = \frac{4\gamma}{D}, \qquad [1]$$

where γ is the surface energy and D is the mean radius of the austenite grains.

In the presence of second phase particles in the matrix, the pinning force exerted on austenite grain boundaries to prevent their migration can be expressed by the well-known Zener pinning force as

$$F_{\mathrm{PIN}} = \beta\frac{\gamma f}{r}, \qquad [2]$$

where β is a dimensionless constant, f is the volume fraction of the second phase particles, r is the mean particle radius and can be replaced by $r = \left(\frac{3f}{4\pi N}\right)^{1/3}$ (where N is the particle volumetric number density, $N = 1/\lambda^3$, and λ is the inter-particle spacing), so that

$$F_{\mathrm{PIN}} = \frac{\beta}{\lambda}\left(\frac{4}{3}\pi\right)^{1/3} f^{2/3}\gamma. \qquad [3]$$

β/λ is defined as a pinning parameter in the present study and related to the precipitates distribution and their relative positions with respect to the austenite grain boundaries.

Maalekian *et al.*[6] reported that a Zener limiting austenite grain size is reached rapidly after reheating the specimen to different temperatures in the range of 1223 K to 1523 K (950 °C to 1250 °C) by Gleeble simulated weld thermal cycle. For simplicity in the

analysis of the present study, it is assumed that a Zener limiting austenite grain size is reached in CGHAZ, *i.e.*, $F_{DRI} = F_{PIN}$, resulting in the following:

$$\frac{4}{D_{lim}} = \frac{\beta}{\lambda}\left(\frac{4}{3}\pi\right)^{1/3} f^{2/3}. \quad [4]$$

Although both (Ti, Nb)N-Nb(C, N) and delayed strain-induced Nb(C, N) impose Zener pinning force that restricts grain boundaries movement, complete dissolution of delayed stain-induced Nb(C, N) and partial dissolution of (Ti, Nb)N-Nb(C, N) occur upon heating to peak temperature above 1573 K (1300 °C) in the region of CGHAZ immediately adjacent to the fusion lines. Therefore, only retained (Ti, Nb)N-Nb(C, N) composite precipitates are taken into account in the calculation.

The volume fraction of (Ti, Nb)N-Nb(C, N) composite precipitate remaining in the CGHAZ of the high-C steel is calculated to be 0.0013 in Section IV–A. Taking experimentally, the observed average austenite grain diameter of 34 μm in the CGHAZ of the high-C steel as D_{lim} in Eq. [4], $\frac{\beta}{\lambda}$ is determined to be 6.12 μm^{-1}. Since the dispersion of (Ti, Nb)N-Nb(C, N) composite precipitates in the two investigated steels are comparable, the same pinning parameter $\frac{\beta}{\lambda}$ is applicable in the calculation for the low-C steel. Based on the volume fraction of (Ti, Nb)N of 0.00068, the Zener limiting austenite grain size in CGHAZ of the low-C steel is calculated to be 52 μm, which is in good agreement with experimentally observed average austenite grain size of 54 μm as shown in Figure 2(b). Although higher solute Nb in CGHAZ of the low-C steel is presumed to impart a stronger solute drag effect on the mobility of austenite grain boundaries than a lower solute Nb does in the CGHAZ of the high-C steel,[28] a higher volume fraction of (Ti, Nb)N-Nb(C, N) remaining in the CGHAZ of the high-C steel exerts a larger Zener pinning pressure on austenite grain boundary, leading to a finer limiting austenite grain size in the CGHAZ of the high-C steel than that in the low-C steel.

Banerjee *et al.*[5] and Maalekian *et al.*[6] reported investigations on non-isothermal austenite grain coarsening kinetics in a similar Ti-Nb microalloyed steel where precipitates coarsening is negligible in the case of a rapid thermal cycle characteristic of low heat input welding. Gong *et al.*[27] reported higher stability of (Ti, Nb)(C, N) than Nb(C, N), and therefore slower dissolution kinetics of Nb in (Ti, Nb)(C, N) than in Nb(C, N) at a high temperature. This can actually be attributed to the lower free energy of the mixed (Ti, Nb)(C, N), regardless of phase separation of TiN and NbC, when compared with NbC alone.[29] (Ti, Nb)N-Nb(C, N) composite precipitates are obtained by promoting epitaxial growth of Nb(C, N) on pre-existing (Ti, Nb)N particles. As shown in Eq. [4], the Zener limiting austenite grain size in CGHAZ can be decreased by reducing the inter-particle spacing λ and increasing the precipitate volume fraction f. To prevent coarsening of austenite grains in CGHAZ, independent control of a small λ by promoting TiN dispersion and a large f by promoting epitaxial growth of Nb(C, N) on pre-existing TiN particles through control of chemistry and processing of the base metal is underscored out of the present study.

C. *Effect of C on Phase Transformation and Associated Variants Configuration*

Salient differences in the morphology and crystallography of the structure in CGHAZ between the low-C and high-C steels indicate that the C content plays a significant role in controlling the final structure. This is in agreement with the well-known fact that C has significant hardenability effect. Even though solute Nb is also reported to be effective in increasing the hardenability,[30,31] the transformation in the CGHAZ of the low-C steel containing less C (0.028 wt pct) and more Nb (0.084 wt pct) in solution as confirmed by APT occurred at a higher temperature with quasi-polygonal ferrite, as shown in Figure 6(a). By comparison, the overall effect of a higher C (0.055 wt pct) and less Nb (0.033 wt pct) in solution in the CGHAZ of the high-C steel promotes bainite transformation at a lower temperature.

Each individual ferrite grain or bainitic lath has a certain crystallographic orientation. The density and dispersion of high-angle boundaries in the final structure are determined by the configuration of crystallographic orientations. In the absence of mechanical deformation in CGHAZ, the nucleation of ferrite upon transformation occurs dominantly from prior austenite grain boundaries. A certain orientation with a semi-coherent low-energy interface with the parent austenite grain is preferred for ferrite nuclei at austenite grain boundary to reduce the nucleation energy barrier.[32] This specific lattice relationship between the ferrite nuclei and the parent austenite grain is maintained by subsequent coherent growth of ferrite into the parent austenite grain,[33] but altered by incoherent growth of ferrite across the austenite boundary into neighboring austenite grains.[34] It is well established that ferrite coherent growth occurs following nearly the Kurdjumov–Sachs (K–S) and Nishiyama–Wassermann (N–W) relationship with respect to its parent austenite grain.[35,36] In reverse, whether a structure is obtained by transformation in coherent mode can be verified by comparing the experimental EBSD (001) pole figure for the structure formed in a single austenite grain with the standard distribution of (001) poles of the 24 variants of the K–S and 12 variants of N–W orientation relationship from the austenite grain with the same orientation.[37,38] Usually, occurrence of a coherent transformation within austenite grains renders prior austenite grain boundaries visible in a final microstructure. In the present study, apparent prior austenite grain boundaries in Figures 6(a) and (b) indicate coherent transformation in CGHAZ of both the low-C and high-C steels.

Upon coherent transformation, a prior austenite grain is divided into four packets, the group of variants with the same parallel close packed planes relationship with respect to the austenite grain, and a packet contains

crystallographic block(s) bounded by high-angle misorientation boundaries.[35,36] Each block consists of sub-blocks associated with variant(s) with the same parallel ⟨001⟩ axes relationship with respect to the parent austenite grain, namely belonging to same Bain group. Figures 12(a) through (c) and (d) through (f) show EBSD all Euler, packet, and Bain maps for the structure formed within the austenite grains delineated in Figures 6(c) and (d) for the low-C and high-C steels, respectively. The colors in the packet and Bain maps are changed to show different packets and Bain groups. The intra-granular needle-like ferrite observed in the CGHAZ of the high-C steel in Figure 6(b) turns out to be bainitic ferrite belonging to a different packet from that of the surrounding matrix. The black and white lines in each map, respectively, show boundaries with misorientation angle above 45 deg and Σ1 boundaries featured as rotation by 10.5 deg about ⟨110⟩ axis. When the packet and Bain group maps are compared, it is found that a packet contains only one Bain group and hence there are no high-angle boundary in the CGHAZ of the low-C steel, whereas in the CGHAZ of the high-C steel, most packets consist of all three Bain groups and therefore it exhibits a high number density of high-angle boundaries. The difference in the density and dispersion of high-angle boundaries in the CGHAZ between the low-C and high-C steels arises from different arrangement of crystallographic variants upon coherent transformation. This, in turn, is controlled by variants selection during ferrite nucleation, which is reported by Furuhara and Takayama *et al*. to be predominately influenced by the transformation driving force and temperature.[39,40] For a small driving force at a high temperature, few nucleation sites are activated and a specific variant is selected in order to minimize the energy barrier for nucleation.[41] In a condition of a large driving force at a low temperature, a difference in activation energy for nucleation between different variants becomes small and more nuclei associated with different variants are promoted at a given austenite grain boundary. The configuration of multiple variants is controlled predominately by self-accommodation of transformation strain arising from the neighboring nucleus.[40,42]

The difference in variant configuration in the CGHAZ between the low-C and high-C steels is thus interpreted in terms of the effect of varying C content on transformation driving force and temperature. C as a strong austenite stabilizer, although an increased C content on the one hand decreases the driving force for ferrite nucleation at a given transformation temperature by stabilizing the austenite,[39] non-equilibrium segregation of C to austenite grain boundaries during fast continuous cooling decreases the transformation temperature by suppressing the nucleation of ferrite. This, on the other hand, increases the driving force for transformation. The overall effect of increased C content is to enhance the driving force for transformation in fast continuous cooling by decreasing the transformation temperature, which promotes more variants during ferrite nucleation. With respect to variant configuration, Σ1 boundary-related V1/V4-type variant pair within a packet and V1/V8-type variant pair forming a packet boundary are preferred at a high transformation temperature in the CGHAZ of the low-C steel, whereas high-angle boundary related two variants belonging to different Bain groups, preferentially V1/V2-type twin-related variant pair is promoted in addition to V1/V4 pair in a packet to self-accommodate transformation strain in the CGHAZ of the high-C steel.[39,40,43-45]

There has been a controversy in the growth mechanism of ferritic component of bainite by C diffusional and partitionless mode, which leads to a difference in the extent of C enrichment in residual austenite.[46,47] The presence of the C-enriched regions in bainitic ferrite due to trapping of C at the dislocations revealed by APT indicates a diffusionless growth of bainitic ferrite, according to Bhadeshia *et al*.[15,19] SADP analysis on the thin films located at bainitic inter-lath boundaries confirms full martensite, indicating its low-C content that is inadequate to stabilize the retained austenite at a low temperature. Combing the TEM observation of the bainitic structure with martensite films occurring at inter-lath boundaries and the EBSD characterization of crystallographic orientation of bainite structure, two schematic diagrams are given in Figures 13(a) and (b) to illustrate the microstructure and associated variants configuration in the CGHAZ of the high-C steel, respectively. While the twin-related variant pairs are promoted by a large driving force for coherent transformation at a low temperature, C is partitioned subsequently into residual austenite sandwiched between adjacent variants, which give rise to martensite films after cooling to room temperature. Finely dispersed martensite films at inter-lath boundaries suppress the occurrence coarse MA particles in CGHAZ. This martensitic thin film is effective in deflecting microcrack propagation by *in situ* TEM studies according to Zhong *et al*.[48]

Lee *et al*.[49] reported that refinement of austenite grain accelerates the kinetics of bainite transformation during continuous cooling. Refined austenite grains in the CGHAZ of the high-C steel due to increased C content enables bainite transformation, which suppresses the brittle martensite formation during fast cooling. Additionally, although a high-C content is contained in the high-C steel, fine MA particles are observed in inter-critically reheated CGHAZ (IRCGHAZ) in the high-C steel. This was attributed to the reduced austenite grain size in the CGHAZ of the high-C steel. This had formed the basis for a design of a laboratory experiment to verify the effect of austenite grain size in CGHAZ on refinement of MA particles in IRCGHAZ, which has been reported elsewhere in Reference 50.

To summary, Figure 14 presents a schematic diagram to show the system responses raised by variation of carbon concentration in base chemistry, including precipitation and dissolution of Ti/Nb carbo-nitrides, austenite grain coarsening, hierarchical evolution of the microstructure morphology, and associated crystallographic variants configuration in the CGHAZ of the two steels.

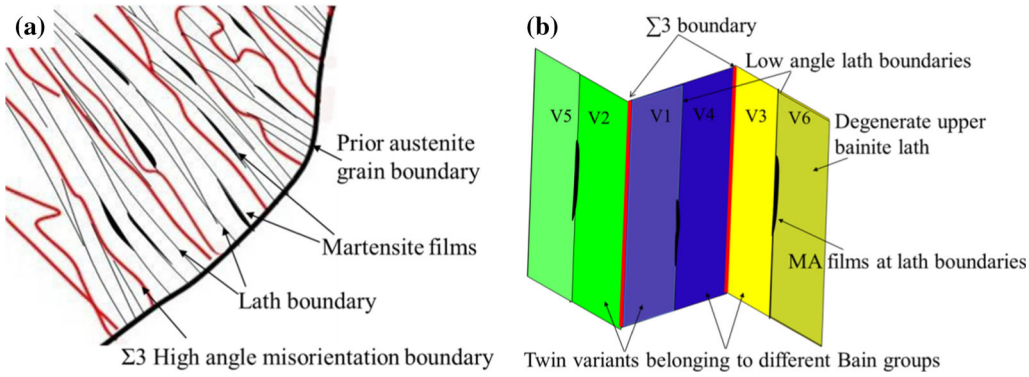

Fig. 13—Schematic illustration describing (*a*) distribution of Σ3 high-angle boundaries indicated by red lines and intermittent martensite films at low-angle sub-block boundaries, (*b*) proposed configuration of crystallographic variants associated with bainitic laths emanating from austenite boundary in the CGHAZ of the high-C steel. While green, blue, and yellow represent variants belonging to different Bain groups, light and dark colors indicate two variants belonging to same Bain group in a packet (Color figure online).

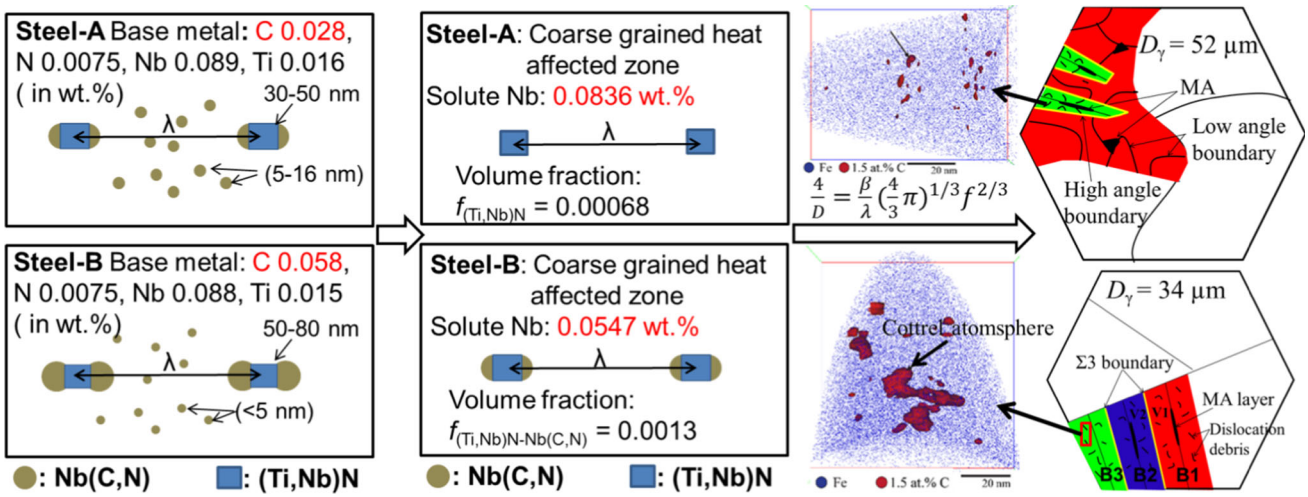

Fig. 14—Schematic diagram showing the effects of carbon content variation on the precipitation and dissolution of Ti/Nb carbo-nitrides, austenite grain coarsening, hierarchical evolution of the microstructure morphology, and associated crystallographic variants configuration in the CGHAZ of the two steels (Color figure online).

V. CONCLUSIONS

The present study examined the HAZ microstructure sensitivity to C content in base chemistry of Ti-Nb microalloyed steels. The effects of varying the C content from 0.028 to 0.058 wt pct on morphology and crystallography of the microstructure in CGHAZ of multi-pass low heat input girth welded steels with the same other chemistry and welding parameters are investigated. The work aims to convey the concept of "system response" raised by one parameter through taking C variation in base chemical composition as an example, other than recommending a specific C content design. The following conclusions specific to the present study are obtained:

(1) The effect of increasing C from 0.028 to 0.058 wt pct is to increase the start temperature of thermodynamic potential for precipitation of NbC by 60 K (60 °C). This promotes more epitaxial growth of Nb(C, N) on pre-existing (Ti, Nb)N particles at high temperatures in the base metal of the high-C steel compared to the low-C steel. In consequence, the high-C steel exhibits larger (Ti, Nb)N-Nb(C, N) of 50 to 80 nm, but smaller delayed strain-induced precipitates of NbC mostly below 5 nm than the low-C steel, which contains (Ti, Nb)N-Nb(C, N) and strain-induced NbC in size range of 30 to 50 and 5 to 16 nm, respectively.

(2) In the CGHAZ immediately adjacent to the fusion line, almost all Nb dissolves into solution in the low-C steel, whereas about 0.033 wt pct Nb remains in (Ti, Nb)N-Nb(C, N) composite precipitates in the high-C steel after thermal cycle of low heat input girth welding. Strain-induced NbC is ineffective in preventing austenite grain coarsening in CGHAZ due to its fast dissolution. For a given inter-spacing originally determined by (Ti, Nb)N particles, an increased volume fraction of (Ti, Nb)N-Nb(C, N) due to more epitaxial growth of Nb(C, N) on pre-existing (Ti, Nb)N in the high-C steel exerts a larger Zener pinning pressure

to prevent austenite grain coarsening, thereby resulting in a finer limiting austenite grain size of 34 μm in CGHAZ of the high-C steel than that of 52 μm in CGHAZ of the low-C steel. Independent control of a short inter-particle spacing by promoting TiN dispersion and a large size/volume fraction by promoting epitaxial growth of NbC on pre-existing TiN particles through control of chemistry and processing of the base metal is identified as an effective approach to control austenite grain coarsening in CGHAZ.

(3) The effect of increasing the C content from 0.028 to 0.058 wt pct is to promote within austenite grains coherent transformation at a lower transformation temperature. The resulting microstructure is composed of bainitic lath structure of 0.5 μm in thickness with intermittent martensite films of 30 to 100 nm in thickness at inter-lath boundaries. Trapping of C at dislocation debris as Cottrell atomspheres with local C concentration in the range of 5 to 9 at. pct in bainitic ferrite and the martensitic nature of the films at bainite inter-lath boundaries indicate the growth of bainite ferrite in diffusionless mode.

(4) The effect of increasing the C content is to promote a high density and uniform dispersion of high-angle misorientation boundaries. This is attributed to the configuration of the variants belonging to different Bain groups in the neighbors in a packet. $\Sigma 3$ boundaries brought about by the occurrence of twin-related variant pairs are preferentially formed. C has a pronounced effect on variant selection during coherent transformation by increasing the transformation driving force through decreasing the transformation temperature upon continuous cooling.

ACKNOWLEDGMENTS

The authors wish to express grateful thanks to Dr. Gianluigi Botton, Dr. Glynis de Silveira, Mr. Chris Butcher, Dr. Andreas Korinek for help with EBSD and TEM characterization of the samples, Mrs. Julia Huang and Mr. Travis Casagrande for help with FIB preparation of the atom probe samples in Canadian Center of Electron Microscope (CCEM) at McMaster University. The funding from CBMM, Brazil, and Evraz, Inc., NA, Canada is gratefully acknowledged.

ELECTRONIC SUPPLEMENTARY MATERIAL

The online version of this article (https://doi.org/10.1007/s11661-018-4751-8) contains supplementary material, which is available to authorized users.

REFERENCES

1. S. Shanmugam, N.K. Ramisetti, R.D.K. Misra, J. Hartmann, and S.G. Jansto: *Mater. Sci. Eng. A*, 2008, vol. 478, pp. 26–37.
2. I.S. De Bott, L.F.G. De Souza, J.C.G. Teixeira, and P.R. Rios: *Metall. Trans. A*, 2005, vol. 36A, pp. 443–54.
3. A. Lambert-Perlade, A.F. Gourgues, J. Besson, T. Sturel, and A. Pineau: *Metall. Mater. Trans. A*, 2004, vol. 5A, pp. 1039–53.
4. A.D. Batte, P.J. Boothby, and A.B. Rothwell: *Proc. Int. Symp. Niobium 2001*, Orlando, Florida, 2001, pp. 931–58.
5. K. Banerjee, M. Militzer, M. Perez, and X. Wang: *Metall. Mater. Trans. A*, 2010, vol. 41A, pp. 3161–72.
6. M. Maalekian, R. Radis, M. Militzer, A. Moreau, and W.J. Poole: *Acta Mater.*, 2012, vol. 60, pp. 1015–26.
7. T. Gladman and F.B. Pickering: in *Yield, Flow and Fracture of Polycrystals*, T.N. Baker, ed., Applied Science Publishers, London, 1983, pp. 141–98.
8. B.L. Bramfitt and J.G. Speers: *Metall. Mater. Trans. A*, 1988, vol. 21A, pp. 817–29.
9. F. Matsuda, Y. Fukada, H. Okada, C. Shiga, K. Ikeuchi, Y. Horii, T. Shiwaku, and S. Suzuki: *Weld. World/Le Soudage dans le Monde*, 1996, vol. 37, pp. 134–54.
10. C.L. Davis and J.E. King: *Mater. Sci. Technol.*, 1993, vol. 9, pp. 8–15.
11. A. Cottrell: in *Yield, Flow and Fracture of Polycrystals*, T.N. Baker, ed., Applied Science Publishers, London, 1983, pp. 123–29.
12. M. Hillert and L.I. Staffansson: *Acta Chem. Scand.*, 1970, vol. 24, pp. 3618–26.
13. K. Thompson, D. Lawrence, D.J. Larson, J.O. Olson, T.F. Kelly, and B. Gorman: *Ultramicroscopy*, 2007, vol. 107, pp. 131–39.
14. B. Gault, M.P. Moody, J.M. Cairney, and S.P. Ringer: *Atom Probe Microscopy*, Springer, New York, 2012.
15. H.K.D.H. Bhadeshia and J.W. Christian: *Metall. Trans. A*, 1990, vol. 21, pp. 767–97.
16. M. Nemoto: *High Voltage Electron Microscopy*, Academic, New York, 1974, p. 230.
17. H.K.D.H. Bhadeshia and D.V. Edmonds: *Metall. Trans. A*, 1979, vol. 10, pp. 895–907.
18. D. Kalish and M. Cohen: *Mater. Sci. Eng.*, 1970, vol. 6, pp. 156–66.
19. M. Peet, S.S. Babu, M.K. Miller, and H.K.D.H. Bhadeshia: *Scripta Mater.*, 2004, vol. 50, pp. 1277–81.
20. F.G. Caballero, M.K. Miller, S.S. Babu, and C. Garcia-Mateo: *Acta Mater.*, 2007, vol. 55, pp. 381–90.
21. A. Cochardt, G. Schoeck, and H. Wiedersich: *Acta Metall.*, 1955, vol. 3, pp. 533–37.
22. S.V. Subramanian, F. Boratto, J.J. Jonas, and C.M. Sellars: *Proc. Int. Symp. Microalloyed Bar Forg. Steels*, Hamilton, Canada, 1990, pp. 120–36.
23. M.T. Nagata, J.G. Speer, and D.K. Matlock: *Metall. Mater. Trans. A*, 2002, vol. 33A, pp. 3099–3110.
24. H. Zou: Kinetics of Carbonitride Precipitation in Microalloyed Steels. Ph.D. Thesis, McMaster University, Canada, 1991.
25. S.G. Hong, K.B. Kang, and C.G. Park: *Scripta Mater.*, 2002, vol. 46, pp. 163–68.
26. X. Ma, C. Miao, B. Langelier, and S. Subramanian: *Mater. Des.*, 2017, vol. 132, pp. 244–49.
27. P. Gong, E.J. Palmiere, and W.M. Rainforth: *Acta Mater.*, 2015, vol. 97, pp. 392–403.
28. J.W. Cahn: *Acta Metall.*, 1962, vol. 10, pp. 789–98.
29. T. Nishizawa: *The 131st and 132nd Nishiyama Memorial Seminar*, ISIJ, Tokyo, 1990, p. 17.
30. C. Fossaert, G. Rees, T. Maurickx, and H.K.D.H. Bhadeshia: *Metall. Mater. Trans. A*, 1995, vol. 26A, pp. 21–30.
31. G.I. Rees, J. Perdrix, T. Maurickx, and H.K.D.H. Bhadeshia: *Mater. Sci. Eng. A*, 1995, vol. 194, pp. 179–86.
32. C.S. Smith: *Trans. Am. Soc. Met.*, 1953, vol. 45, pp. 533–75.
33. H. Réglé, N. Maruyama, and N. Yoshinaga: *Proc. Int. Conf. Adv. High Strength Sheet Steels Automot. Appl.*, Winter Park, Colorado, 2004, pp. 239–46.
34. M. Hillert: *Decomposition of Austenite by Diffusional Processes*, Interscience, New York, 1972.
35. Z. Guo, C.S. Lee, and J.W. Morris, Jr: *Acta Mater.*, 2004, vol. 52, pp. 5511–18.
36. H. Kitahara, R. Ueji, N. Tsuji, and Y. Minamino: *Acta Mater.*, 2006, vol. 54, pp. 1279–88.

37. Y. You, C. Shang, W. Nie, and S. Subramanian: *Mater. Sci. Eng. A*, 2012, vol. 558, pp. 692–701.
38. Y. You, C. Shang, L. Chena, and S. Subramanian: *Mater. Sci. Eng. A*, 2012, vol. 546, pp. 111–18.
39. T. Furuhara, H. Kawata, S. Morito, and T. Maki: *Mater. Sci. Eng. A*, 2006, vol. 431, pp. 228–36.
40. N. Takayama, G. Miyamoto, and T. Furuhara: *Acta Mater.*, 2012, vol. 60, pp. 2387–96.
41. T. Furuhara, H. Kawata, S. Morito, G. Miyamoto, and T. Maki: *Metall. Mater. Trans. A*, 2008, vol. 39A, pp. 1003–13.
42. V. Pancholi, M. Krishnan, I.S. Samajdar, V. Yadav, and N.B. Ballal: *Acta Mater.*, 2008, vol. 56, pp. 2037–50.
43. S. Morito, H. Tanaka, R. Konishi, T. Furuhara, and T. Maki: *Acta Mater.*, 2003, vol. 51, pp. 1789–99.
44. S. Morito, X. Huang, T. Furuhara, T. Maki, and H. Hansen: *Acta Mater.*, 2006, vol. 54, pp. 5323–31.
45. A. Lambert-Perlade, A.F. Gourgues, and A. Pineau: *Acta Mater.*, 2004, vol. 52, pp. 2337–48.
46. H.K.D.H. Bhadeshia and D.V. Edmonds: *Acta Metall.*, 1980, vol. 28, pp. 1265–73.
47. M. Hillert, L. Höglund, and J. Ågren: *Metall. Mater. Trans. A*, 2004, vol. 35A, pp. 3693–3700.
48. Y. Zhong, F. Xiao, J. Zhang, Y. Shan, W. Wang, and K. Yang: *Acta Mater.*, 2006, vol. 54, pp. 435–43.
49. S.-J. Lee, J.-S. Park, and Y.-K. Lee: *Scripta Mater.*, 2008, vol. 59, pp. 87–90.
50. X. Li, X. Ma, S.V. Subramanian, C. Shang, and R.D.K. Misra: *Mater. Sci. Eng. A*, 2014, vol. 616, pp. 141–47.